

Sulfonic Acid-Functionalized Donor-Acceptor Conjugated Organic Polymer for Enhanced Photocatalytic Hydrogen Peroxide Production

Authors: *Qingxia Zhu^a, Haoxi Wang^a, Xiaobo Luo^a, Wuzi Zhao^a, Danfeng Wang^a,
Shiyuan Zhou^{a*}, Lingyun Xu^{b*}, Guangfeng Liu^{a*}, Peiyang Gu^{a*}*

Affiliations: *^aJiangsu Key Laboratory of Advanced Catalytic Materials and
Technology, School of Petrochemical Engineering, Changzhou University,
Changzhou, 213164, PR China. E-mail address: zhoushiyuan@cczu.edu.cn (S. Zhou);
guangfeng.liu@cczu.edu.cn (G. Liu); gupeiyang0714@cczu.edu.cn (P. Gu).*

*^bAnalysis and Testing Center, Soochow University, Suzhou, 215123, China. E-mail
address: lyxu@suda.edu.cn (L. Xu).*

Contents

1. Methods	S3
1.1 Materials	S3
1.2 Characterization.....	S3
2. Synthetic procedure	S4
2.1 Synthesis of 2,5-bis((trimethylsilyl)ethynyl)pyrimidine	S4
2.2 Synthesis of 2,5-diethynylpyrimidine	S5
2.3 Synthesis of BMO	S6
2.4 Synthesis of BMS	S7
3. Experiments	S8
3.1 Photoelectrochemical measurements.....	S8
3.2 Rotating disk electrode (RDE) measurements	S8
3.3 Photosynthesis of H ₂ O ₂	S9
3.4 ESR experiments	S9
3.5 Isotope labeling experiment	S10
4. Results and discussion	S10
5. References	S24

1. Methods

1.1 Materials

5,10,15,20-Tetrakis(4-bromophenyl)porphyrin, *N,N*-dimethylformamide (DMF), 2,5-dibromopyrimidine, and tetrabutylammonium fluoride (TBAF) were purchased from Shanghai Titan Scientific Co., Ltd. Chlorosulfonic acid, methanol, and dichloromethane were obtained from Sinopharm Chemical Reagent Co., Ltd. Tetrakis(triphenylphosphine)palladium (Pd(PPh₃)₄), tetrahydrofuran (THF, AR, 99.0%), methanol (HPLC grade, ≥ 99.9%), ethanol (AR, 99.0%), and chloroform (AR, 99.0%) were purchased from Shanghai Haohong Biomedical Technology Co., Ltd. 2,2,6,6-Tetramethylpiperidine-1-oxyl (TEMPO, 97.0%), 2,2,6,6-tetramethyl-4-piperidone (TEMP, 97.0%), 5,5-dimethyl-1-pyrroline-N-oxide (DMPO, 97.0%), ethylenediaminetetraacetic acid disodium salt (EDTA-2Na, 99.0%), β-carotene (97.0%), and isopropanol (IPA, AR, 99.5%) were acquired from Shanghai Macklin Biochemical Co., Ltd. Potassium titanyle oxalate, silver nitrate (AgNO₃), and Nafion were purchased from Aladdin. All chemicals were used without further purification.

1.2 Characterization

A Fourier transform infrared (FT-IR) spectrophotometer (Thermo Scientific Co., United States, Nicolet 6700) was used to measure the FT-IR spectra of samples using a KBr pellet. The solid-state ¹³C NMR was measured on a Bruker INOVA 400 MHz NMR spectrometer. The N₂ adsorption-desorption isotherms were performed on a Quantachrome Micromeritics ASAP 2020 instrument at 77 K. Based on the N₂ adsorption-desorption data, the Brunauer-Emmett-Teller (BET) method was used to calculate the specific surface area of the samples. The powder X-ray diffraction (PXRD) of the samples was performed on an X'Pert-Pro MPD analyzer. The surface morphology of COPs is observed by scanning electron microscope (SEM, Merlin Compact, Japan). The hydrophilicity and hydrophobicity of COPs are measured in a water contact angle analyzer. The thermal stability of the materials is tested by thermogravimetric analysis (TGA, TG209F3, Germany) from 30 °C to 700 °C with

the heating rate of 10 °C min⁻¹. The surface chemistry of the catalysts is analyzed by X-ray photoelectron spectroscopy (XPS, ESCALAB 250, USA). The concentration of the H₂O₂ was calculated based on the absorbance at 400 nm by a UV-vis spectrophotometer. The absorption of COPs at solid state was measured by a UV-Vis spectrophotometer (Shimadzu, UV3600). Electrochemical properties were studied by an electrochemical workstation (CHI760E, Shanghai, China). The signals of active radicals were detected by an electron spin resonance (ESR) spectrometer (JEOL, JES-X320).

2. Synthetic procedure

2.1 Synthesis of 2,5-bis((trimethylsilyl)ethynyl)pyrimidine

A mixture of 2,5-dibromopyrimidine (6.25 g, 28.07 mmol) and trimethylsilylacetylene (22.68 g, 230.4 mmol) was dissolved in THF (90 mL) and anhydrous triethylamine (50 mL). Under a N₂ atmosphere, CuI (1.086 g, 5.7 mmol), PPh₃ (1.02 g, 3.8 mmol), and Pd(PPh₃)₂Cl₂ (1.2 g, 1.7 mmol) were sequentially added. The reaction mixture was then heated to 50 °C and refluxed for 24 h. The progress of the reaction was monitored by a thin-layer chromatography (TLC). After completion, the mixture was cooled to room temperature, poured into water, and extracted with dichloromethane. The product was purified by column chromatography, yielding 4 g of the desired product with a yield of 52.3%. ¹H NMR (400 MHz, CDCl₃) δ 8.71 (s, 2H), 0.25-0.28 (d, *J* = 8.3 Hz, 18H).

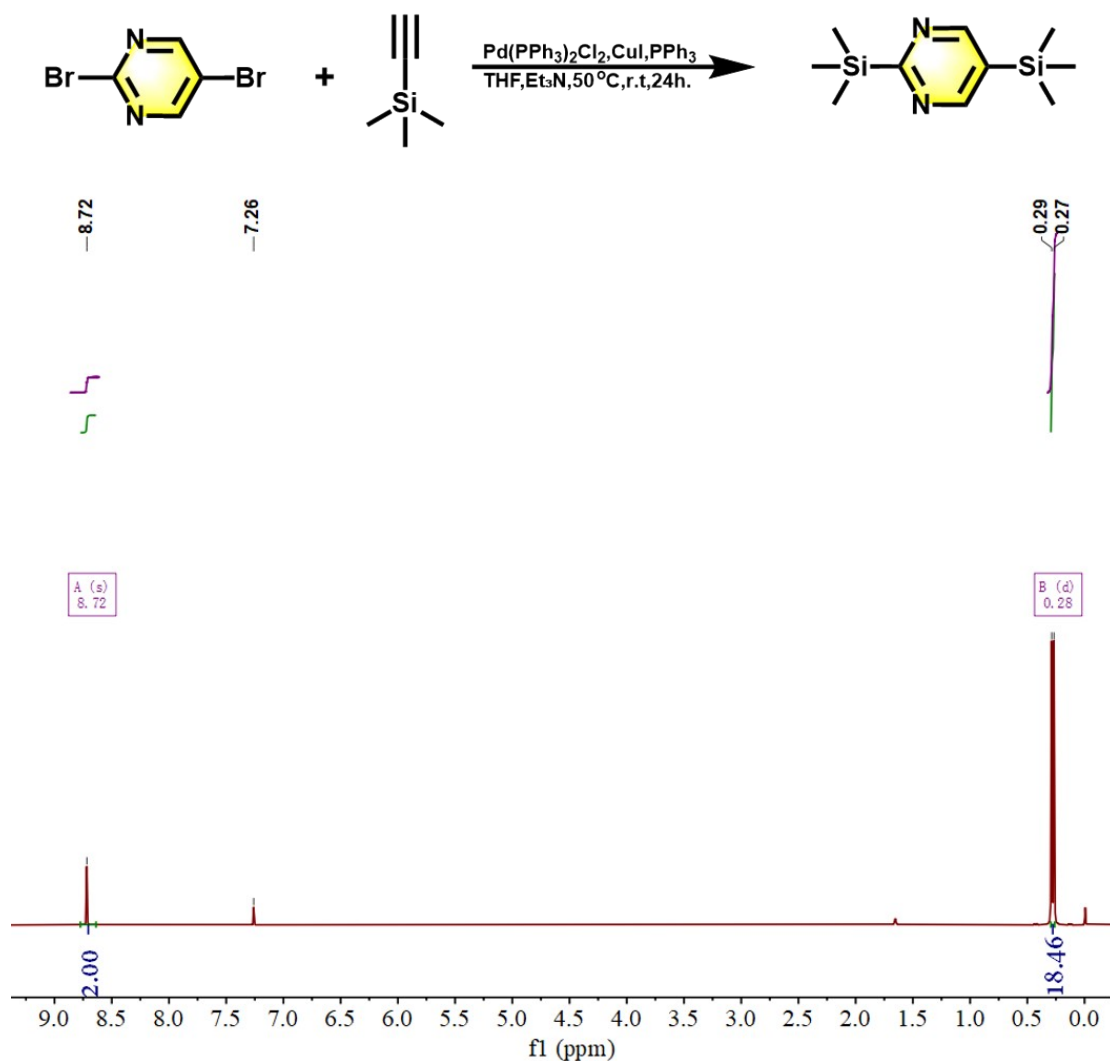


Fig. S1 The synthetic procedure and the ¹H NMR spectrum of 2,5-bis((trimethylsilyl)ethynyl)pyrimidine).

2.2 Synthesis of 2,5-diethynylpyrimidine

Under a N₂ atmosphere, 2,5-bis((trimethylsilyl)ethynyl)pyrimidine (3.8 g, 13.9 mmol) was dissolved in 50 mL of THF. Tetrabutylammonium fluoride (TBAF) was slowly added dropwise at -40 °C, and the reaction progress was monitored by TLC. After the reaction was completed, the mixture was cooled to room temperature, poured into water, and extracted with dichloromethane. The product was purified by column chromatography, yielding 1.3 g of the desired product with a yield of 73%. ¹H NMR (400 MHz, CDCl₃) δ 8.79 (s, 2H), 3.49 (s, 1H), 3.27 (s, 1H).

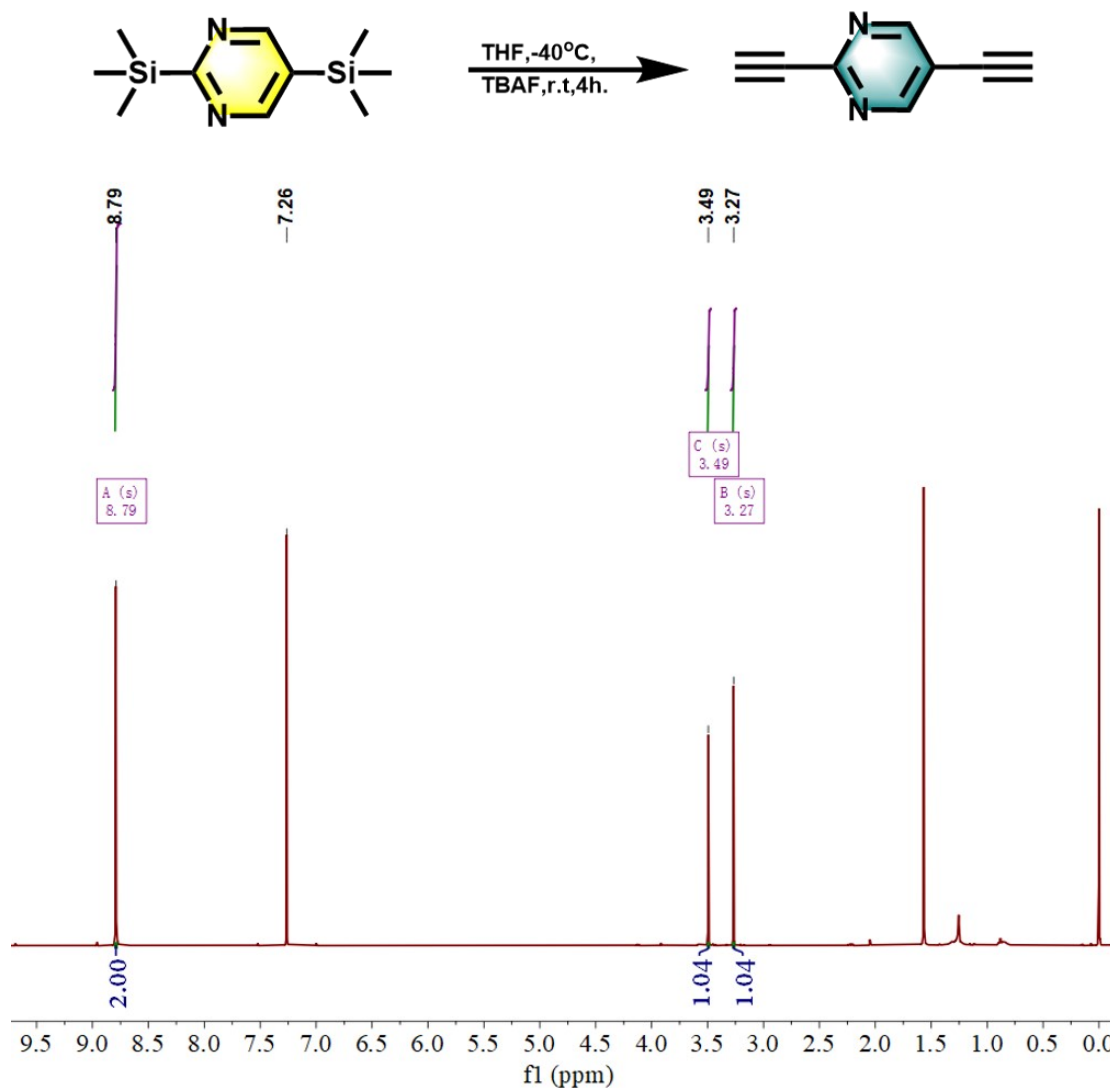
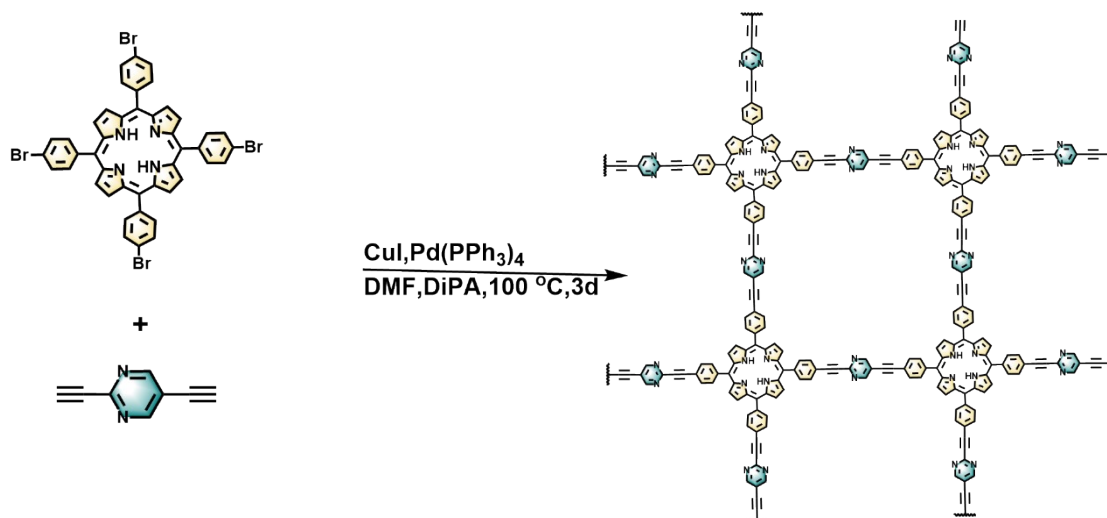


Fig. S2 The synthetic procedure and the ¹H NMR spectrum of 2,5-diethynylpyrimidine.

2.3 Synthesis of BMO

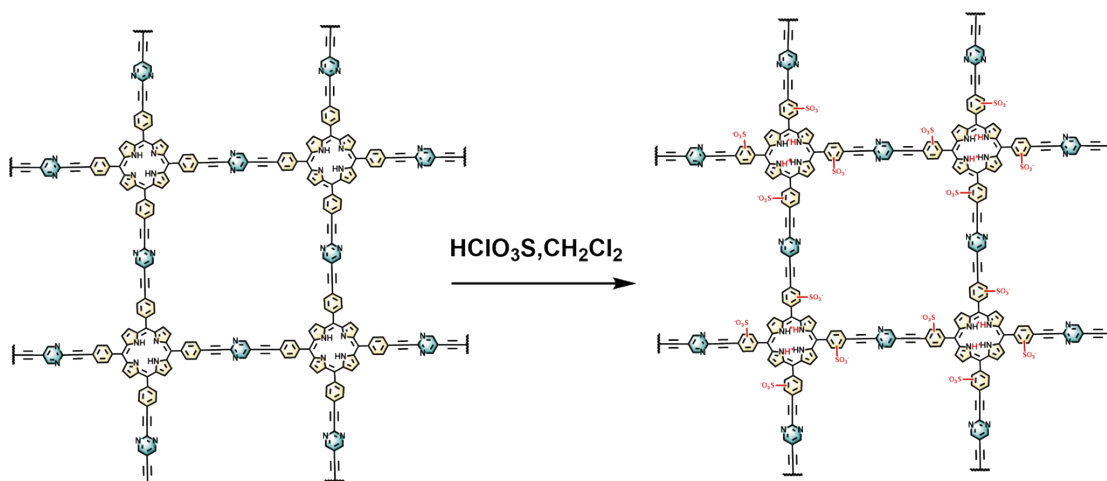
5,10,15,20-Tetrakis(4-bromophenyl)porphyrin (2.78 g, 3 mmol) and 2,5-diethynylpyrimidine (762 mg, 6 mmol) were dissolved in 200 mL of DMF and 100 mL of diisopropylamine in a 500 mL Schlenk flask. After purging with N₂ for 10 min, CuI (114.2 mg, 0.6 mmol) and Pd(PPh₃)₄ (277 mg, 0.24 mmol) were added. The mixture was heated to 100 °C and reacted for 3 d at a N₂ atmosphere. After the reaction was completed, the mixture was cooled to room temperature and filtered to collect the solid product. The crude product was successively Soxhlet extracted with

THF, dichloromethane, and methanol to yield a dark purple solid namely BMO (2.3 g, yield of 68 %).



2.4 Synthesis of BMS

BMO (600 mg) was dispersed in 50 mL of anhydrous dichloromethane in a 250 mL Schlenk flask. 12 mL of chlorosulfonic acid was dropwise added in an ice bath at a N_2 atmosphere. The mixture was stirred at room temperature for 48 h. After the reaction was completed, the mixture was filtered and successively washed with deionized water and methanol to obtain a reddish-brown solid namely BMS (640 mg).



3. Experiments

3.1 Photoelectrochemical measurements

For Mott-Schottky, transient photocurrent response, and electrochemical impedance spectroscopy (EIS) measurements, a three-electrode system was employed. Briefly, 5 mg of the sample was dispersed in 2 mL of ethanol, followed by the addition of 20 μL Nafion solution. The mixture was sonicated to ensure homogeneous dispersion of the catalyst. Subsequently, 200 μL of the suspension was drop-cast onto an ITO glass substrate (1 cm \times 2 cm \times 0.1 cm) to fabricate the working electrode. An Ag/AgCl electrode and a platinum sheet were used as the reference electrode and counter electrode, respectively. A 0.1 M aqueous solution of sodium sulfate served as the electrolyte. A 600 W Xenon lamp was utilized as the light source for photocurrent measurements.

3.2 Rotating disk electrode (RDE) measurements

In this experiment, a three-electrode system was employed with a CHI700 electrochemical workstation (CH Instruments). The RDE setup consisted of a glassy carbon disk working electrode, a Pt ring electrode, and an Ag/AgCl reference electrode. For the preparation of the catalyst-loaded working electrode, 4 mg of the catalyst and 1 mg of carbon black were dispersed in a mixture of 600 μL deionized water, 320 μL isopropanol, and 80 μL Nafion solution. The mixture was sonicated for 30 min to obtain a homogeneous suspension. Subsequently, 9.4 μL of the suspension was deposited onto a freshly polished glassy carbon electrode and allowed to be dried under ambient conditions. A 1 M KOH solution was prepared as the electrolyte. Prior to electrochemical measurements, the electrolyte was purged with oxygen for 30 min to achieve oxygen saturation. Cyclic voltammetry (CV) was first performed to record the current-potential relationship, with multiple cycles conducted to ensure data stability. Linear sweep voltammetry (LSV) measurements were then carried out at rotation speeds of 500, 1000, 1500, 2000, and 2500 rpm, respectively.

Electrochemical measurements: The number of electrons transferred during the oxygen reduction reaction (ORR) process was determined using the Koutecky-Levich equation, as shown in Equations (1) and (2):

$$\frac{1}{j} = \frac{1}{j_K} + \frac{1}{j_L} = \frac{1}{j_K} + \frac{1}{B\omega^{1/2}} \quad (1)$$

$$B = 0.62nFC_0 D^{2/3} \nu^{-1/6} \quad (2)$$

Where j is the measured current density, j_K and j_L are kinetic and diffusion-limited current densities, ω is the angular velocity, n is the number of transferred electrons, F is the Faradaic constant (96485 C/mol), C_0 is the volume concentration of O_2 (0.84×10^{-3} mol/L), D_0 is the diffusion coefficient of O_2 in 1 M KOH (1.65×10^{-5} cm²/s), ν is the dynamic viscosity of the electrolyte (0.01 cm²/s).

3.3 Photosynthesis of H₂O₂

5 mg of photocatalyst was dispersed in 20 mL of ultrapure water and ultrasonicated to obtain a homogeneous suspension. The resulting mixture was transferred to a reactor and subjected to magnetic stirring and continuous illumination using a 600 W Xenon lamp. The total irradiation duration was set to 60 min. 2 mL of the suspension was collected at 10, 20, 30, 40, 50, and 60 min, then filtered through a 0.22 μ m hydrophilic PET membrane to remove the photocatalyst. The filtrate was mixed with a pre-prepared potassium titanium oxalate solution (0.02 M), then the absorbance at 400 nm was measured using a UV spectrophotometer to determine the H₂O₂ concentration. For experiments involving different atmospheres, the system was first purged with O₂ or N₂ in the dark to achieve saturation. Subsequently, the reaction was irradiated with a continuous supply of O₂ or N₂.

3.4 ESR experiments

2.5 mg of photocatalyst was dispersed in 1 mL of ultrapure water and 1 mL of methanol, respectively, followed by ultrasonication for 20 min. Different trapping

agents were selected for the detection of various active species. For h^+ and e^- , 200 μL of the test solution was mixed with 200 μL of TEMPO (200 μM) aqueous solution. For $^1\text{O}_2$, 200 μL of the test solution was mixed with 200 μL of TEMP (200 μM) aqueous solution. For $\bullet\text{OH}$, 200 μL of the test solution was mixed with 200 μL of 100 mM DMPO aqueous solution. For $\bullet\text{O}_2^-$, 200 μL of the test solution was mixed with 200 μL of 100 mM DMPO methanol solution. A capillary tube was used to draw 50 μL of each mixture, which was then placed into the ESR instrument. The samples were firstly tested in the dark for 1 min, followed by irradiation with a xenon lamp. Signals were recorded at 1 min and 3 min of light exposure, respectively.

3.5 Isotope labeling experiment

BMS was suspended in H_2^{18}O (0.5 mL) in a 1.5 mL transparent glass vial and sonicated for 1 min. The suspension was purged with N_2 for 5 min in the darkness and sealed off before being irradiated for 1 h. The headspace was analyzed by GC-MS.

4. Results and discussion

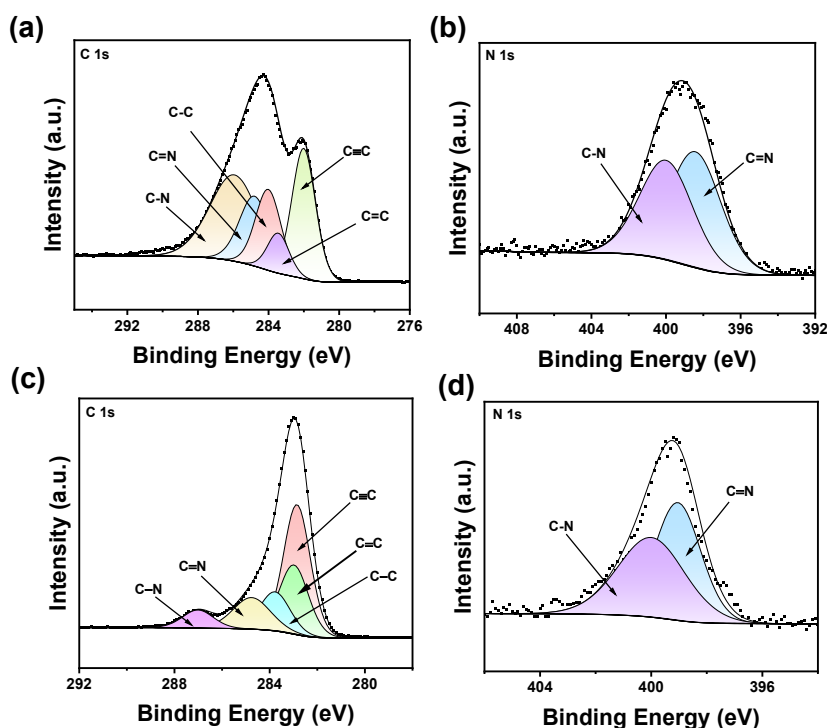


Fig. S3 The C 1s and N 1s high-resolution XPS spectra of (a-b) BMO and (c-d) BMS.

The morphology of the two polymers was characterized using scanning electron microscopy (SEM) (**Fig. S4-S5**). The results indicate that both BMO and BMS exhibit typical spherical morphologies. SEM mapping analysis clearly reveals the uniform distribution of C, N, O, and S elements within the BMS, further confirming the successful introduction of sulfonic acid groups. This finding is consistent with the results in XPS analysis.

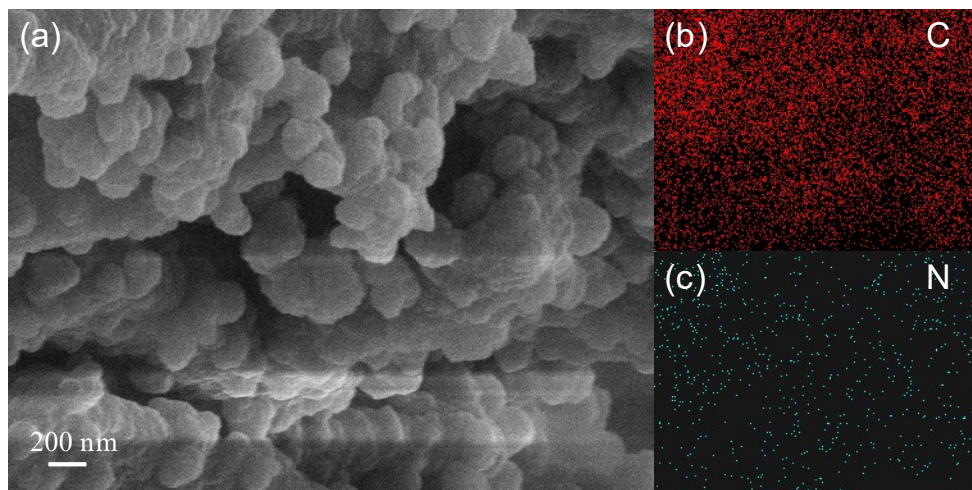


Fig. S4 The (a) SEM images and (b-e) SEM mapping of BMO. C: red; N: green.

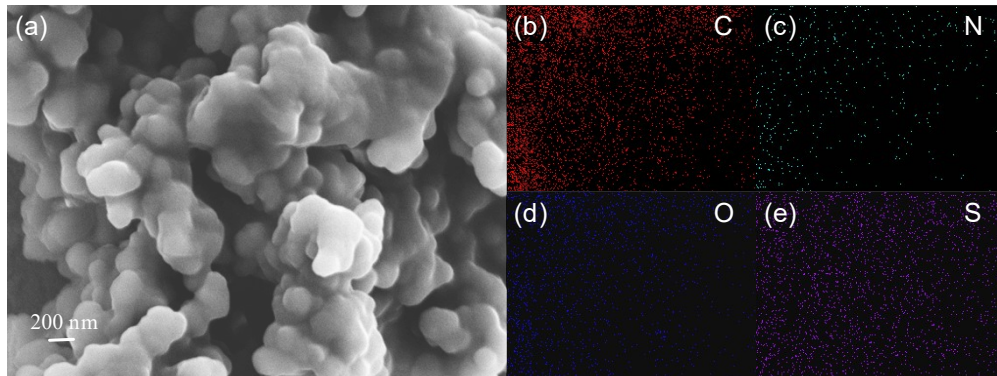


Fig. S5 The (a) SEM images and (b-e) SEM mapping of BMS. C: red; N: green; O: blue; S: purple.

Additionally, the X-ray diffraction (XRD) results (**Fig. S6**) show that both BMO and BMS exhibit broad diffraction peaks around 20° , confirming their amorphous natures.

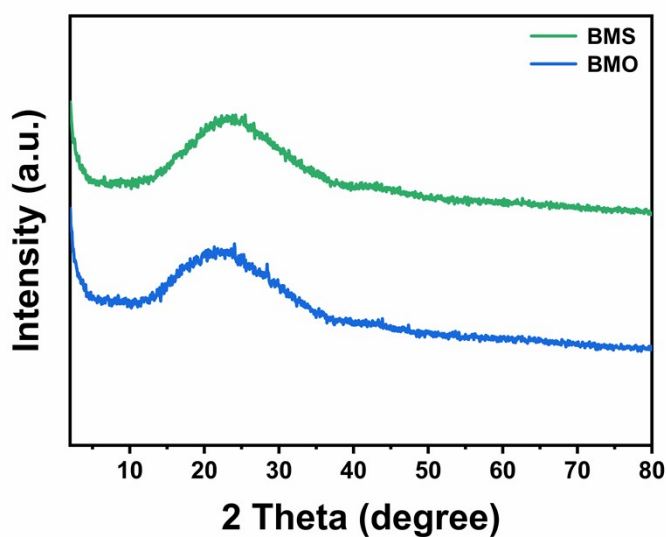


Fig. S6 The XRD curves of BMO and BMS.

The water contact angle measurements (**Fig. S7**) reveal that the modification of $-\text{SO}_3\text{H}$ groups has significantly improved the hydrophilicity ($\theta_{\text{BMO}}=120^\circ$, $\theta_{\text{BMS}}=10^\circ$). Enhanced hydrophilicity provides better dispersion and contact, with promotes the diffusion of reactant molecules (*e.g.* O_2 and H_2O).

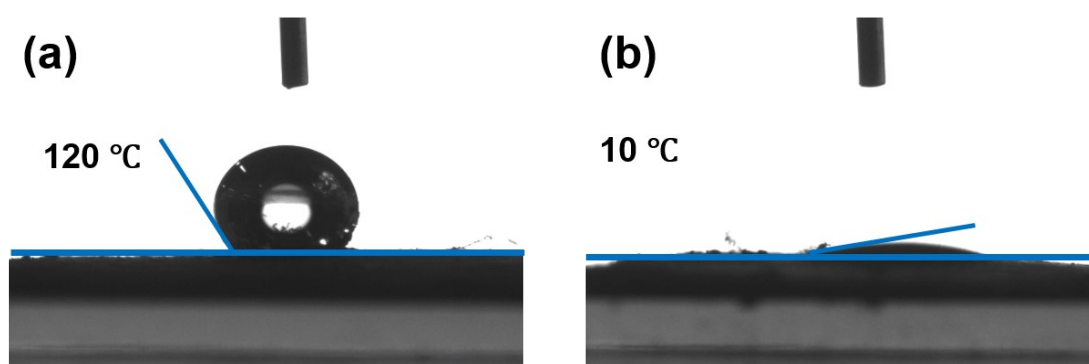


Fig. S7 The water contact angles of (a) BMO and (b) BMS.

Moreover, the zeta potentials of BMO and BMS are measured as 11.3 mV and -43.8 mV, respectively under neutral conditions, indicating that BMS exhibits stronger charge affinity for protons (**Fig. S8**).

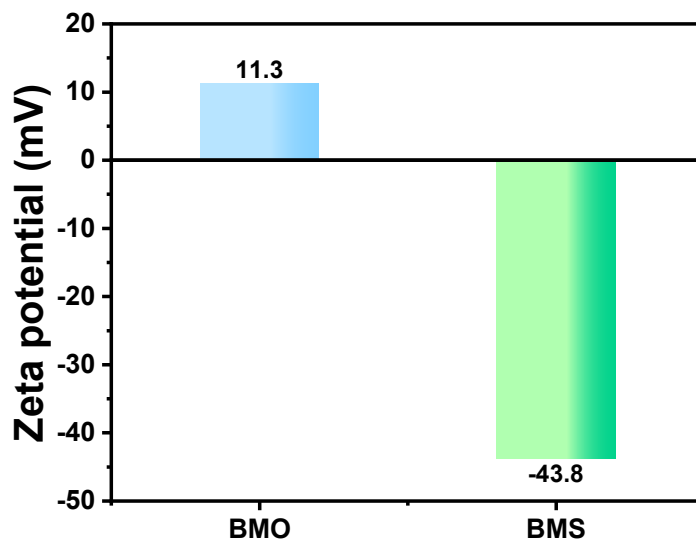


Fig. S8 The Zeta potentials of BMO and BMS.

The thermal gravimetric analysis (TGA) in **Fig. S9** showed that the temperatures corresponding to a 5% mass loss are 151 °C for BMO and 172 °C for BMS, demonstrating their excellent thermal stability.

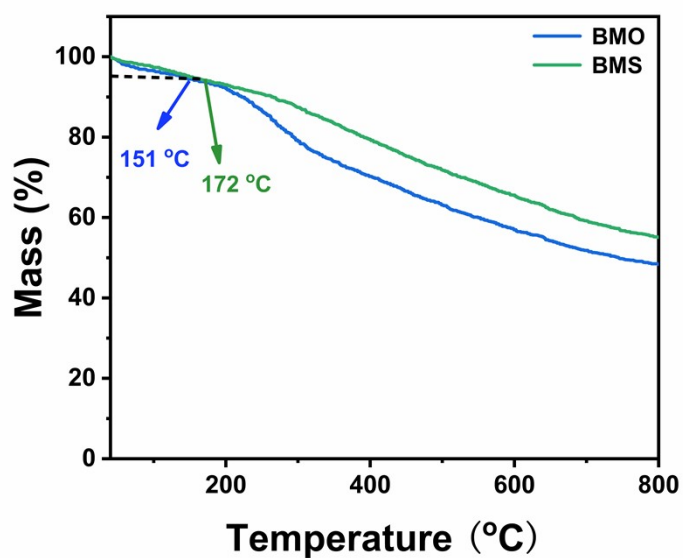


Fig. S9 The TGA curves of BMO and BMS.

Additionally, as shown in **Fig. S10**, the N₂ adsorption-desorption isotherms reveal that BMO and BMS both exhibit type II isotherms with Brunauer-Emmett-Teller (BET) surface areas of 13 and 22 m²/g, respectively. The

average pore sizes of BMO and BMS are 16.63 nm and 11.62 nm, respectively, indicating that both materials possess a mesoporous structure.

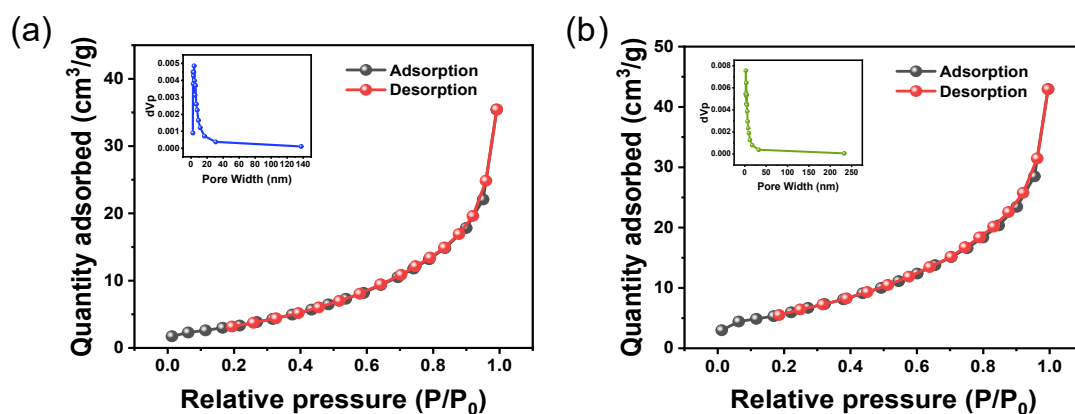


Fig. S10 The BET curves of (a) BMO and (b) BMS. Inset: the corresponding pore size distributions.

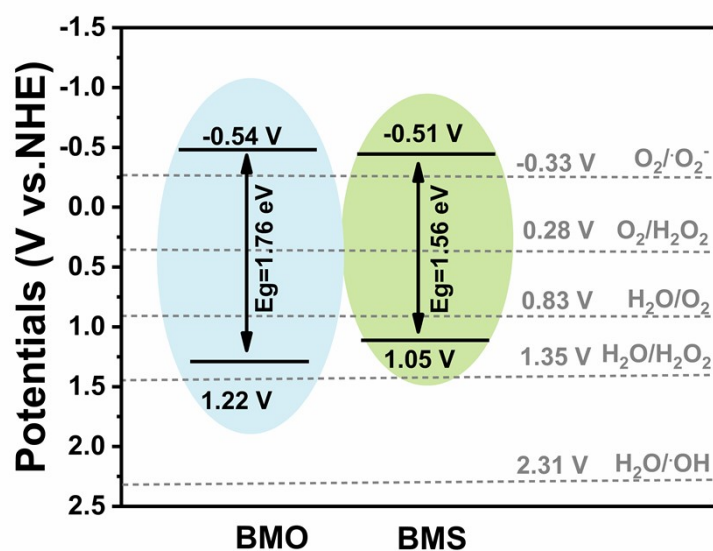


Fig. S11 Band structures of BMO and BMS.

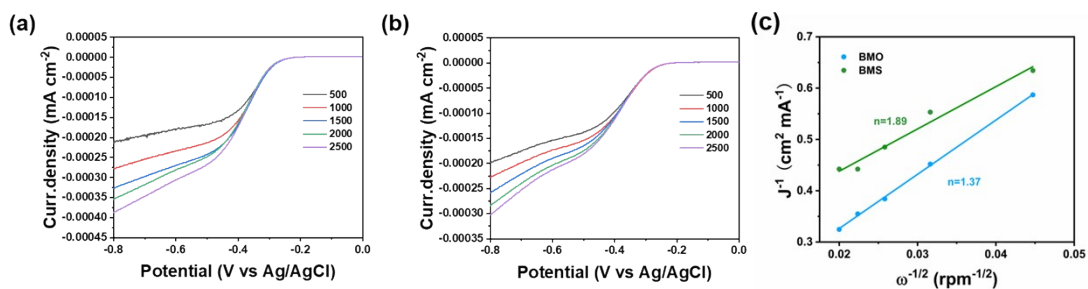


Fig. S12 The linear-sweep rotating disk electrode voltammograms of (a) BMO and (b) BMS. Unit: Hz. (c) Koutecky-Levich plots of BMO and BMS.

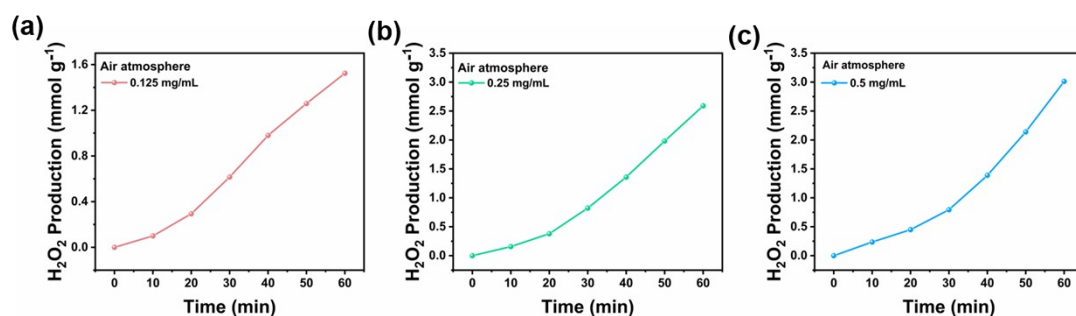


Fig. S13 The time-course plots of H_2O_2 concentration with different dosages of BMS.

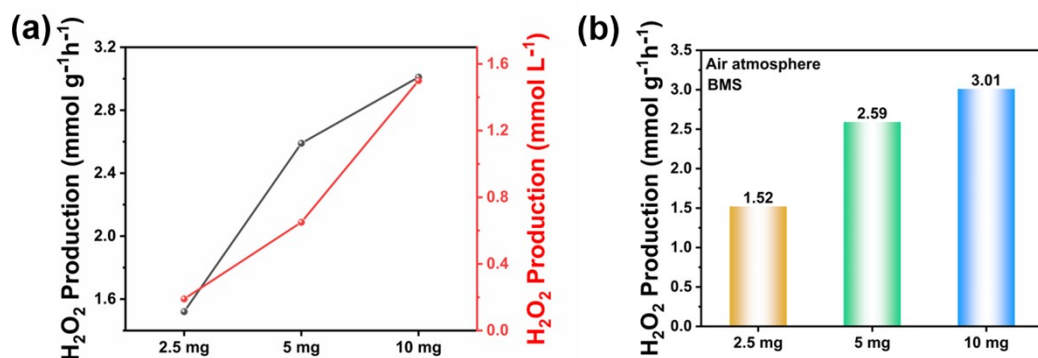


Fig. S14 (a) the corresponding curves of H_2O_2 yield versus H_2O_2 production rate with different photocatalyst dosages for BMS; (b) The effect of different BMS dosages on the H_2O_2 production rate.

As illustrated in **Fig. S15**, under dark conditions, the H_2O_2 production was almost negligible ($< 0.1 \text{ mmol g}^{-1} \text{ h}^{-1}$), confirming the photo-driven nature of the reaction. When using a 420 nm cutoff filter, BMS maintained excellent photocatalytic performance with an H_2O_2 production rate of $2.12 \text{ mmol g}^{-1} \text{ h}^{-1}$, which not only verifies the visible-light-driven mechanism but also highlights the catalyst's exceptional visible light utilization capability. Furthermore, control experiments using

the monomer precursor (5,10,15,20-tetra(4-ethynylphenyl)porphyrin) yielded only minimal H₂O₂ production (0.39 mmol g⁻¹ h⁻¹) under identical conditions, providing definitive evidence that the observed catalytic activity originates from the polymeric structure of BMS rather than any residual monomers or impurities.

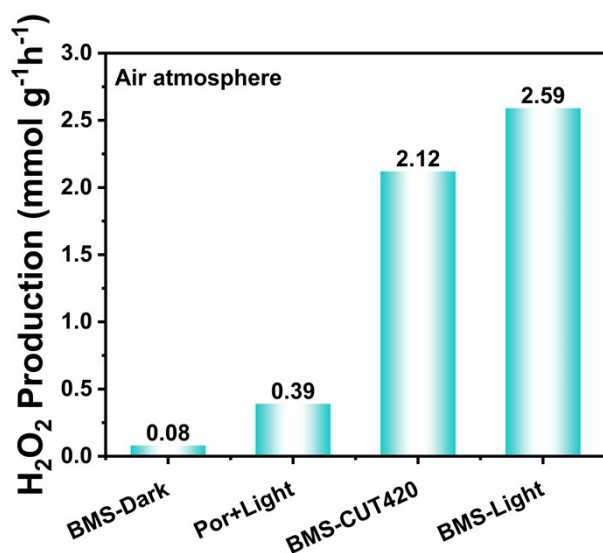


Fig. S15 Effects of different conditions on photocatalytic H₂O₂ production.

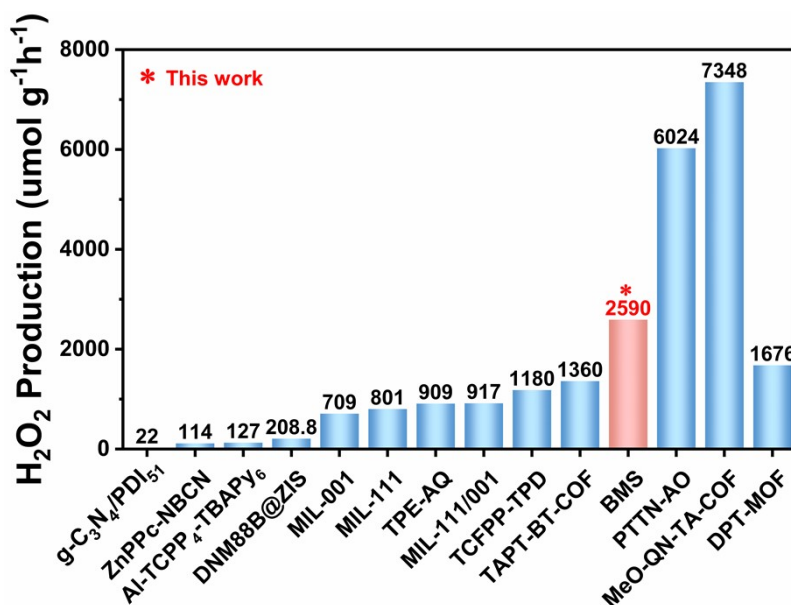


Fig. S16 Comparisons on the H₂O₂ production rate of BMS with previous reports.

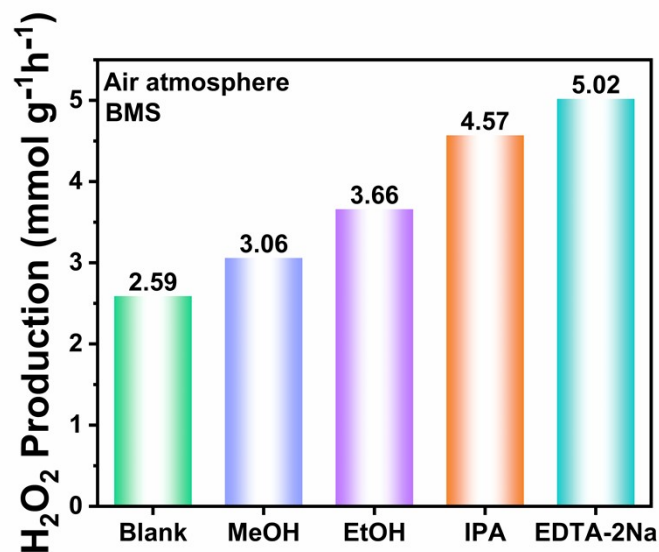


Fig. S17 The H₂O₂ production of BMS in the presence of different sacrificial agents in air.

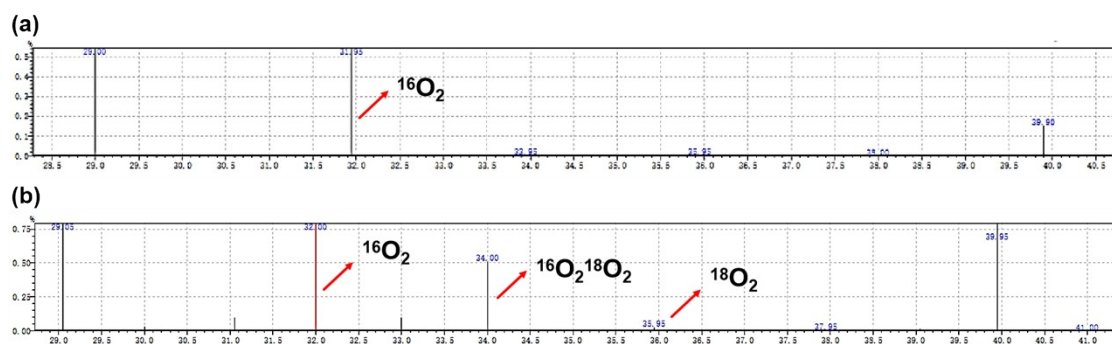


Fig. S18 The GC-MS of (a) O₂ and (b) the headspace after 1 h of irradiation for BMS.

To provide a clear visualization of the relative contributions of ORR and WOR in the photocatalytic production of H₂O₂, **Fig. S19** presents a schematic illustration. The results demonstrate that ORR plays a dominant role in this process, while within the WOR mechanism, the 4e⁻-WOR pathway contributes more significantly than the 2e⁻-WOR pathway.

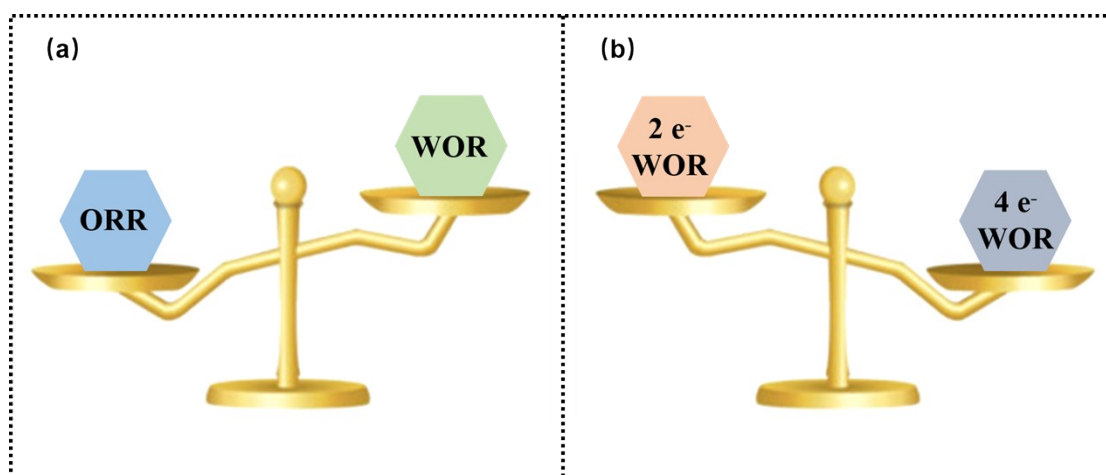


Fig. S19 (a) The importance of ORR and WOR in the hydrogen peroxide production process. (b) Comparison of the significance between $4e^-$ WOR and $2e^-$ WOR in the WOR mechanism.

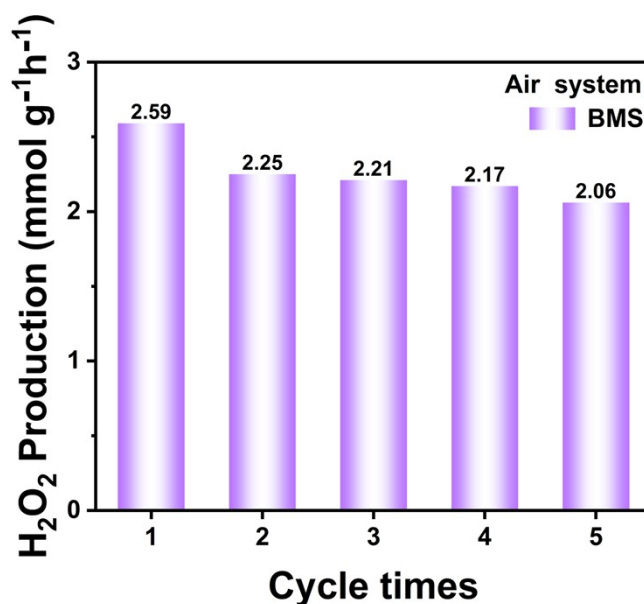


Fig. S20 The photocatalytic H_2O_2 production performance of BMS achieved within 5 cycles.

We have collected BMS after five cycles and it was characterized by FT-IR and XPS. In the FT-IR spectra (**Fig. S21**), the characteristic peaks of the alkyne group ($-C\equiv C-$) at $2362\ cm^{-1}$ and the stretching vibrations of $O=S=O$ at $1115\ cm^{-1}$ and $1011\ cm^{-1}$ remained clearly observable. The absence of new absorption bands indicated no bond cleavage or functional group degradation in the bulk structure, demonstrating that BMS remained intact under prolonged illumination, with the $-SO_3H$ groups

exhibiting exceptional chemical stability. Furthermore, as shown in **Fig. S22**, the XPS analysis of recycled BMS confirmed the retention of C, N, S, and O element, verifying that the sulfonic acid groups are preserved within the COPs. These results collectively underscore the robust structural stability of the BMS, even after photocatalytic cycling.

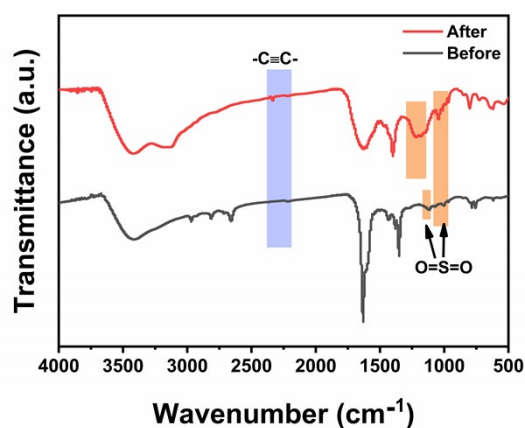


Fig. S21 FT-IR spectra of BMS before and after photocatalytic reaction.

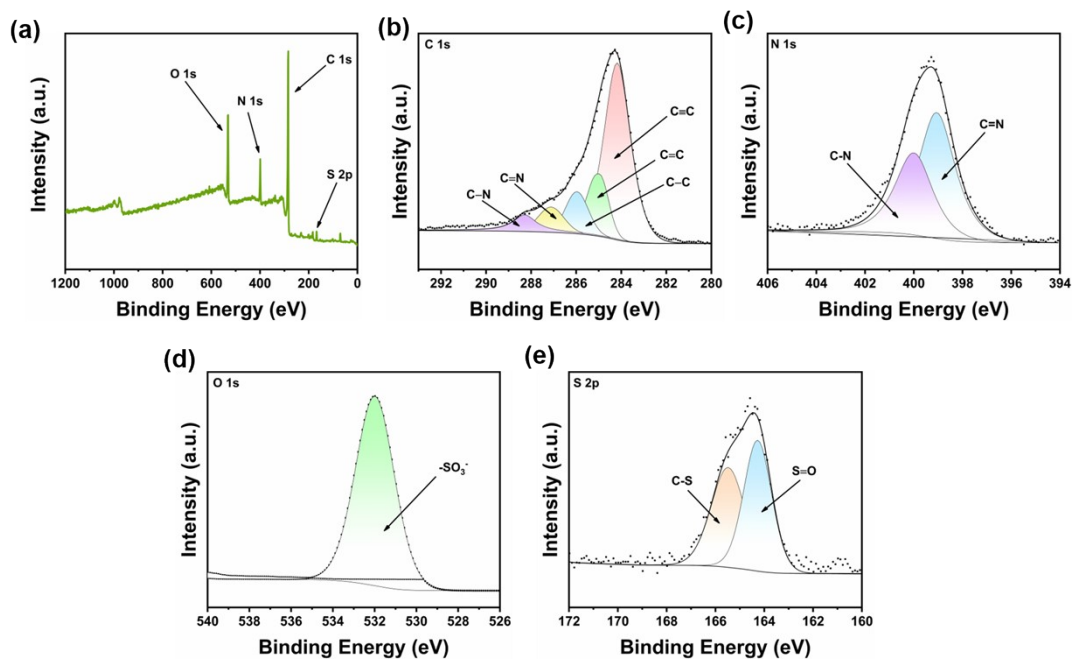


Fig S22 XPS spectra of the photocatalyst after recycling tests: (a) full XPS spectra of BMS. (b)-(e) the C 1s, N 1s, O 1s, and S 2p high-resolution XPS spectra of BMS after five cycles.

The TEMPO, 2,2,6,6-tetramethyl-4-oxopiperidine (TEMP) were employed as the spin-trapping agents for h^+ and 1O_2 , and the 5,5-dimethyl-1-pyrroline *N*-oxide (DMPO)

was for $\bullet\text{OH}$ and $\bullet\text{O}_2^-$. As shown in **Fig. S23**, except for TEMP-h^+ , almost no signals were observed in the darkness. However, under illumination, the characteristic quadruplex peaks of $\text{DMPO-}\bullet\text{OH}$, sextet peaks of $\text{DMPO-}\bullet\text{O}_2^-$, and triplet signals of $\text{TEMP-}^1\text{O}_2$ were observed, confirming the generation of these ROS. While for TEMP-h^+ , the intensity of its triplet peaks was gradually decreased with prolonged irradiation time, indicating that the h^+ has been consumed.

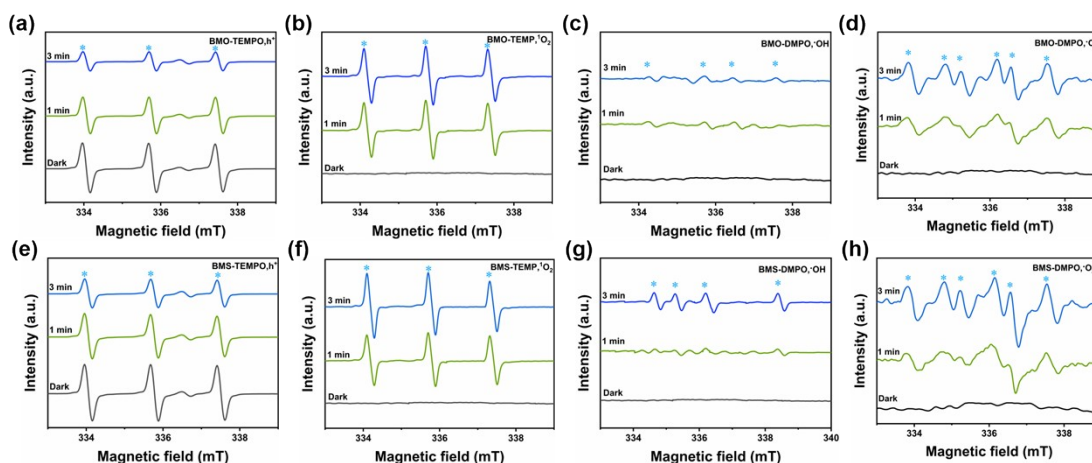


Fig. S23 (a-d) The ESR spectra of TEMP-h^+ , $\text{TEMP-}^1\text{O}_2$, $\text{DMPO-}\bullet\text{OH}$, $\text{DMPO-}\bullet\text{O}_2^-$ for BMO; (e-h) The ESR spectra of TEMP-h^+ , $\text{TEMP-}^1\text{O}_2$, $\text{DMPO-}\bullet\text{OH}$, $\text{DMPO-}\bullet\text{O}_2^-$ for BMS in the darkness and under visible-light irradiation.

Firstly, the highest occupied molecular orbital (HOMO) and the lowest unoccupied molecular orbital (LUMO) of BMO and BMS were calculated (**Fig. S24**). The HOMO and LUMO energy levels exhibit partial overlap, with the HOMOs primarily locate in the pyrrole units of the porphyrin and the pyrimidine units, while the LUMOs are mainly distributed in the porphyrin units. This electronic structure indicates that these materials possess significant donor-acceptor (D-A) characteristics, facilitating the effective separation and transfer of photogenerated carriers.

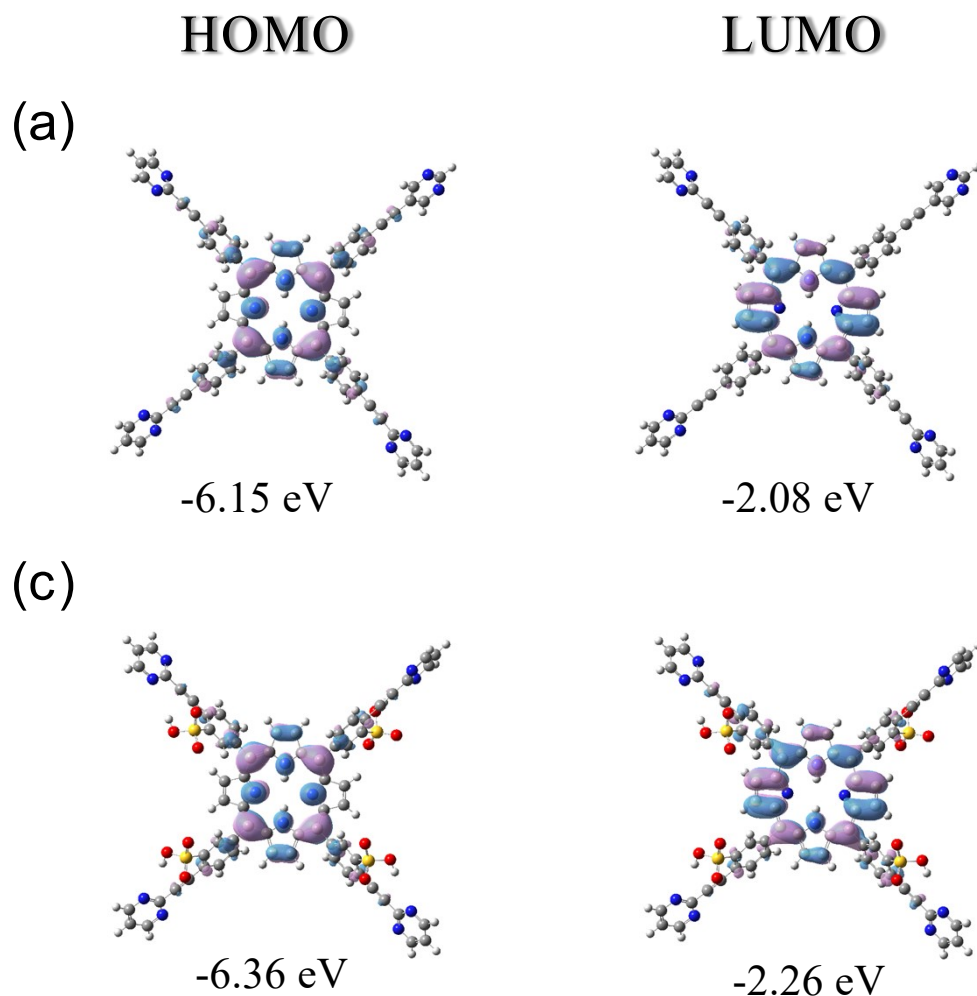


Fig. S24 The HOMO and LUMO of (a) BMO and (b) BMS.

We evaluated the hydrogen peroxide (H_2O_2) production performance of various photocatalysts under standard solar illumination conditions (AM 1.5G). The results demonstrate that the BMS catalyst exhibits exceptional H_2O_2 generation activity, achieving a production rate of $723 \mu\text{mol g}^{-1} \text{h}^{-1}$, which significantly outperforms most reference catalysts (**Table S2**).

Table S1 Comparison of H_2O_2 production performance for diverse polymeric photocatalytic materials

Photocatalysts	Photocatalyst concentration	H_2O_2 production ($\mu\text{mol g}^{-1} \text{h}^{-1}$)	Reaction conditions	Reference
$\text{g-C}_3\text{N}_4/\text{PDI}_{51}$	50 mg catalyst, 30 mL H_2O	22	$\lambda > 420 \text{ nm}$, O_2	1

ZnPPc-NBCN	10 mg catalyst, 20 mL H ₂ O	114	$\lambda > 420$ nm, Air	2
DNM88B@ZIS	30 mg catalyst, 30 mL H ₂ O	208.8	$\lambda > 420$ nm	3
MIL-001	5 mg catalyst, 20 mL H ₂ O	709	$\lambda > 400$ nm	4
MIL-111	5 mg catalyst, 20 mL H ₂ O	801	$\lambda > 400$ nm	4
TPE-AQ	10 mg catalyst, 20 mL H ₂ O	909	$\lambda \geq 400$ nm, 100 mW·cm ⁻²	5
MIL-111/001	5 mg catalyst, 20 mL H ₂ O	917	$\lambda > 400$ nm	4
TCFPP-TPD	10 mg catalyst, 20 mL H ₂ O	1180	$\lambda > 420$ nm, O ₂	6
TAPT-BT-COF	10 mg catalyst, 20 mL H ₂ O	1360	$\lambda > 420$ nm, O ₂	7
PTTN-AO	5 mg catalyst, 50 mL H ₂ O	6024	$\lambda > 420$ nm, O ₂	8
MeO-QN-TA- COF	4 mg catalyst, 20 mL H ₂ O	7384	460 nm blue LED	9
DPT-MOF	5 mg catalyst, 30 mL H ₂ O	1676	300W Xenon lamp, O ₂	10
BMS	5 mg catalyst, 20 mL H₂O	2590	600W Xenon lamp, Air	This work
BMS	10 mg catalyst, 20 mL H₂O	3010	600W Xenon lamp, O₂	This work

Table S2 The comparison of various photocatalysts for photocatalytic H₂O₂ production under simulated sunlight (AM 1.5G, 1 sun).

Photocatalysts	Gas	Photocatalyst concentration	Irradiation conditions	H ₂ O ₂ yield	Reference
COF-N32	O ₂	25 mg 50 ml H ₂ O	natural sunlight	605 $\mu\text{mol g}^{-1} \text{h}^{-1}$	11
BTT-H3	O ₂	5 mg 10 mL H ₂ O	natural sunlight	550 $\mu\text{mol g}^{-1} \text{h}^{-1}$	12

Pd/TiO ₂	Air	10 mg catalyst, 20 mL H ₂ O	AM 1.5G 100W	300 μmol g ⁻¹ h ⁻¹	13
NMT400	O ₂	20 mg catalyst, 50 mL H ₂ O	AM 1.5G 100W	270 μmol g ⁻¹ h ⁻¹	14
TDB-COF	Air	10 mg catalyst, 10 mL H ₂ O	AM 1.5G 300 W	723 μmol g ⁻¹ h ⁻¹	15
BMS	Air	5 mg catalyst, 20 mL H₂O	AM 1.5G 100 W	429 μmol g⁻¹ h⁻¹	This work

5. References

- (1) Shiraishi, Y.; Kanazawa, S.; Kofuji, Y.; Sakamoto, H.; Ichikawa, S.; Tanaka, S.; Hirai, T. *Angew. Chem. Int. Edit.* 2014, **53**, 13454-13459.
- (2) Ye, Y.-X.; Pan, J.; Xie, F.; Gong, L.; Huang, S.; Ke, Z.; Zhu, F.; Xu, J.; Ouyang, G. *Proc. Natl. Acad. Sci.* 2021, **118**, e2103964118.
- (3) Liu, M.; Xing, Z.; Zhao, H.; Song, S.; Wang, Y.; Li, Z.; Zhou, W. *J. Hazard. Mater.* 2022, **437**, 129436.
- (4) Zheng, Y.; Zhou, H.; Zhou, B.; Mao, J.; Zhao, Y. *Catal. Sci. Technol.* 2022, **12**, 969-975.
- (5) Ye, Y.-X.; Pan, J.; Shen, Y.; Shen, M.; Yan, H.; He, J.; Yang, X.; Zhu, F.; Xu, J.; He, J.; *Proc. Natl. Acad. Sci.* 2021, **118**, e2115666118.
- (6) Zhang, R.; Zhao, H.; Pan, C.; Zhang, J.; Jian, L.; Sun, X.; Ji, R.; Li, J.; Dong, Y.; Zhu, Y. *New J. Chem.* 2024, **48**, 3316-3324.
- (1) Shiraishi, Y.; Kanazawa, S.; Kofuji, Y.; Sakamoto, H.; Ichikawa, S.; Tanaka, S.; Hirai, T. *Angew. Chem. Int. Edit.* 2014, **53**, 13454-13459.
- (2) Ye, Y.-X.; Pan, J.; Xie, F.; Gong, L.; Huang, S.; Ke, Z.; Zhu, F.; Xu, J.; Ouyang, G. *Proc. Natl. Acad. Sci.* 2021, **118**, e2103964118.
- (3) Liu, M.; Xing, Z.; Zhao, H.; Song, S.; Wang, Y.; Li, Z.; Zhou, W. *J. Hazard. Mater.* 2022, **437**, 129436.
- (4) Zheng, Y.; Zhou, H.; Zhou, B.; Mao, J.; Zhao, Y. *Catal. Sci. Technol.* 2022, **12**, 969-975.
- (5) Ye, Y.-X.; Pan, J.; Shen, Y.; Shen, M.; Yan, H.; He, J.; Yang, X.; Zhu, F.; Xu, J.; He, J.; *Proc. Natl. Acad. Sci.* 2021, **118**, e2115666118.
- (6) Zhang, R.; Zhao, H.; Pan, C.; Zhang, J.; Jian, L.; Sun, X.; Ji, R.; Li, J.; Dong, Y.; Zhu, Y. *New J. Chem.* 2024, **48**, 3316-3324.
- (7) Wang, L.; Sun, J.; Deng, M.; Liu, C.; Ataberk Cayan, S.; Molken, K.; Geiregat, P.; Morent, R.; De Geyter, N.; Chakraborty, J.; *Catal. Sci. Technol.* 2023, **13**, 6463-6471.
- (8) Yu, Z.; Yu, F.; Xu, M.; Feng, S.; Qiu, J.; Hua, J., *Adv. Sci.* 2025, **12** (14), 2415194.

- (9) Liu, R.; Zhang, M.; Zhang, F.; Zeng, B.; Li, X.; Guo, Z.; Lang, X., *Small*. 2025, **21** (10), 2411625.
- (10) Choi, J. Y.; Check, B.; Fang, X.; Blum, S.; Pham, H. T. B.; Tayman, K.; Park, J., *J. Am. Chem. Soc.* 2024, **146** (16), 11319-11327.
- (11) Liu, F.; Zhou, P.; Hou, Y.; Tan, H.; Liang, Y.; Liang, J.; Zhang, Q.; Guo, S.; Tong, M.; Ni, J., *Nat. Commun.* 2023, **14** (1), 4344.
- (12) Chakraborty, A.; Alam, A.; Pal, U.; Sinha, A.; Das, S.; Saha-Dasgupta, T.; Pachfule, P., *Nat. Commun.* 2025, **16** (1), 503.
- (13) Chu, C.; Huang, D.; Zhu, Q.; Stavitski, E.; Spies, J. A.; Pan, Z.; Mao, J.; Xin, H. L.; Schmuttenmaer, C. A.; Hu, S.; Kim, J.-H., *ACS Catal.* 2019, **9** (1), 626-631.
- (14) Yang, C.; Wan, S.; Zhu, B.; Yu, J.; Cao, S., *Angew. Chem., Int. Ed.* 2022, **61** (39), e202208438.
- (15) Zhou, Z.; Sun, M.; Zhu, Y.; Li, P.; Zhang, Y.; Wang, M.; Shen, Y., *Appl. Catal., B.* 2023, **334**, 122862.